Journal of Applied Fluid Mechanics, Vol. 18, No. 12, pp. 2968-2987, 2025.
Available online at www.jafmonline.net, ISSN 1735-3572, EISSN 1735-3645.
https://doi.org/10.47176/jafm.18.12.3652

Rotating Stall Characteristics in the Hump Region of a Pump Turbine: Application of Modal Decomposition

Y. H. Zhang[1], J. L. Wang[1], W. T. Su[2], Y. Zhao[3, 4], Y. L. Chen[3, 4], T. P. Chen[3, 4] and J. Wu[1†]

[1] *School of Energy Science and Engineering, Harbin Institute of Technology, Harbin 150001, China*
[2] *School of Petroleum and Natural Gas Engineering, Liaoning Petrochemical University, Fushun Liaoning 113001, China*
[3] *Harbin Electric Machinery Company Limited, Harbin 150040, China*
[4] *Harbin Institute of Large Electric Machinery, Harbin 150040, China*

†Corresponding Author Email: jian.wu@hit.edu.cn

ABSTRACT

A reversible pump turbine is a large-scale commercial energy storage device that serves as the core component of a pumped storage power station. Under pump operating conditions, the reversible pump turbine often exhibits hump characteristics on the head–discharge performance curve, leading to operational instability and limiting both regulation performance and safety. However, the mechanism underlying flow instability in the hump region is not adequately understood. Existing analysis methods are limited in scope, and they struggle to identify key flow structures accurately in application. In this study, large eddy simulation (LES) is used to investigate unsteady flow characteristics under typical hump conditions. Proper orthogonal decomposition (POD) and dynamic mode decomposition (DMD) methods are applied to a transient flow field to extract dominant modal structures and analyze their dynamic behaviors. The results show that rotating stalls in the guide vane and runner regions are the primary factors creating hump characteristics. Both the POD and DMD methods effectively capture major vortex structures and their changes, demonstrating their suitability for analyzing complex flow dynamics. These findings provide theoretical insight into the flow instability mechanism in the hump region and offer guidance for improving the operational performance of pump turbines.

Article History

Received May 5, 2025
Revised July 4, 2025
Accepted July 18, 2025
Available online October 6, 2025

Keywords:

Pump-turbine
Numerical simulation
Complex flow field
Rotating stall
Modal decomposition

1. INTRODUCTION

Considering the global transition toward clean and low-carbon energy, hydropower, as a major source of renewable energy, plays an irreplaceable role in power regulation and energy structure optimization (François et al., 2016; Mohsin et al., 2023; Wu, 2023; Karapici et al., 2024). Among various technologies, reversible pump turbines serve as the core components of pumped storage power stations. The reversible pump turbine undertakes tasks such as peak shaving, frequency regulation, and phase balancing, thereby enhancing grid stability (Mahfoud et al., 2023; Subramanya & Chelliah, 2023 Wang et al., 2023a). During peak electricity demand, this component operates as a turbine to generate power, whereas during off-peak periods, it reverts to functioning as a pump, converting electrical energy into stored potential energy. Similar to a large-scale power bank, the reversible pump turbine effectively compensates for the intermittency and fluctuation characteristics of renewable energy sources (Jin et al., 2023; Hao et al., 2024). Compared with conventional energy storage technologies, pump turbines offer advantages such as long service lives, high efficiencies, and minimal environmental impacts (Nasir et al., 2022; Yin et al., 2023).

Owing to the complex structure of the unit and the frequent switching between operating conditions, various transient instabilities still occur during actual power plant operation. These issues are particularly significant under unstable conditions, such as low flow rates and rotational speeds, where the efficiency and safety of the pump turbine are easily compromised (Lai et al., 2023; Liang et al., 2024; Zhang et al., 2024). Therefore, investigating the mechanisms underlying such instabilities is essential. As illustrated in Fig. 1, under complex operating scenarios and during short load regulation or frequency control cycles, the unit inevitably passes through the hump region, where the slope of the head–discharge curve becomes positive. If the flow rate increases under such conditions, the pump head rises along the hump curve and

NOMENCLATURE

POD	Proper Orthogonal Decomposition	q	DMD mode matrix
DMD	Dynamic Mode Decomposition	w	decay rate of DMD modal index
u	velocity	f	frequency
$\bar{u}_i$	mean velocity	b	initial condition matrix
u'	fluctuating velocity	C_S	Smagorinsky constant
x	section coordinate point	Δ	filter width
t	time	$\lvert \bar{S} \rvert$	strain rate tensor
N	number of time samples	τ_{ij}	sub-grid scale stress
m	number of spatial samples in section	v_T	eddy viscosity coefficient
B	POD spatial mode matrix	H	pump head
S	diagonal matrix of eigenvalues	η	pump efficiency
V	mode construction matrix	Q	flow rate
λ	eigenvalue	ΔP	total pressure loss
a	temporal coefficient (mode amplitude)	*num*	mode number
U'	fluctuating velocity matrix over time	*EW*	energy weight of each mode
U	velocity matrix over time	*TEW*	Total Energy Weight
A	linear mapping operator	Real	real part of eigenvalue
$\tilde{A}$	reduced-order linear operator	Imag	imaginary part of eigenvalue
fn	rotational frequency of the pump		

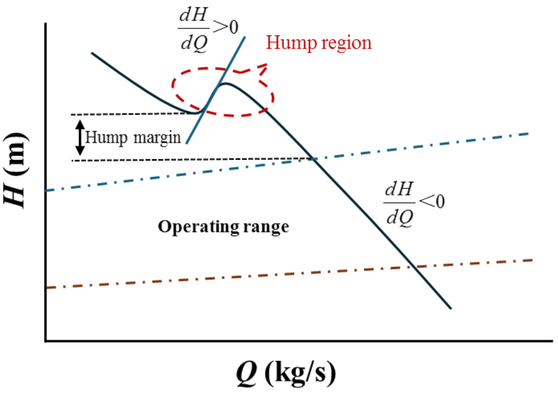

Fig. 1 Hump characteristics in pump mode

potentially exceeds the system head, causing the fluid to retain excess energy after passing through the machine. This residual energy accelerates the flow, further increasing the discharge level and driving the operating point away from its original position. As a result, the performance of the pump turbine deteriorates significantly, leading to intensified instability, pronounced pressure fluctuations, and severe internal flow disturbances (Ye et al., 2024; Zheng et al., 2024).

Xu et al. (2024) conducted PIV tests on pump turbine systems and observed significant vortex structures in the impeller and guide vane passages, which block the flow channels. The scholars confirmed that rotational stall was a critical factor contributing to hydraulic instability in the hump region. Qin et al. (2023) described the complex vortex evolution process, specifically focusing on rotational stall, occurring in the impeller-free region of pump turbine systems; this process was closely linked to the formation of an unstable region in the hump region of the pump. Li et al. (2018) analyzed the dynamics of flow fields and hydraulic losses. The researchers reported that the hump characteristics and associated hysteresis phenomena arose from the increased hydraulic losses. These losses were caused by vortices in the guide vane region and backflow near the shroud side of the impeller inlet. Further studies by Liu et al. (2024) revealed that vortex structures under pump mode reduced the channel flow rate and increased the hydraulic losses. As the flow rate decreased, the rising head could not offset head loss, which resulted in an increased slope of the head curve and the appearance of a positive local slope, thereby forming a hump region. The backflow effect significantly contributed to hydraulic losses and was a key factor in hump formation.

In flow field analysis, modal decomposition is an important approach for constructing reduced-order models. This process helps extract dominant features from complex flows and reduce system dimensionality (Sieber et al., 2016; Wang et al., 2023b). This method facilitates the understanding of unsteady flow behavior by revealing the coupling characteristics among various physical quantities in fluid dynamics (Proctor et al., 2016; Rowley & Dawson, 2017; Towne et al., 2018). POD extracts spatially orthogonal dominant modes by ranking flow field data on the basis of energy content (Liao et al., 2020; Renhui et al., 2020). In contrast, DMD involves the temporal evolution characteristics of physical quantities. DMD can be considered to identify characteristic frequencies, reveal the influences of different frequency components on the flow field, and predict the changes in flow structures over time (Mariappan et al., 2014; Arbabi & Mezic, 2017; Schmid, 2022).

Lumley (1967) was the first to apply the POD method to the study of turbulent coherent structures. As a mathematical approach capable of effectively extracting structures related to the dynamic states of the flow field, POD decomposes the flow field to identify modal structures that describe the main behavioral features of the flow, facilitating the analysis of complex flow phenomena. Building upon this technique, Sirovich (1987) proposed the snapshot POD method, which collects flow field data at different time instances as snapshot samples, transforming the spatial dimension of the original POD algorithm into the time domain. This approach solved the problem associated with high-dimensional matrices that was difficult to address at the time, and it had greatly reduced computational costs. Yang et al. (2023) employed the POD method to study the frequency and spatial intensity distribution characteristics of stall cells under various operating conditions. The scholars revealed that energy losses in the guide vane region significantly influenced the formation of humps on the performance curve. Schmid (2010) introduced the DMD method to the fluid dynamics field. On the basis of Koopman's analysis method, DMD is a relatively novel data processing technique that analyzes the temporal changes in flow fields by using the eigenvalues of dynamic modes, thus identifying the main features and modal behaviors of flow. Liu et al. (2019b) investigated the transient characteristics of gas–liquid two-phase flow in rotating multiphase pumps. By using the DMD method, the researchers decoupled the coherent structures of the multiphase flow field and identified the coherent structures of liquid and gas velocities at the midplane between the guide vane and impeller.

Earlier, Muld et al. (2012) successfully extracted primary flow structures in the wake of high-speed trains via both the POD and DMD methods and studied the convergence of these methods from relevant aspects. Magionesi et al. (2018) employed both the POD and DMD methods to study flow characteristics in the wake of ship propellers. The scholars reported that both methods could identify the wake instability caused by the coupling of continuous tip vortices, the interactions between the impeller and tip vortices, and the wake oscillation mechanism. In further research, Taira et al. (2020) reported that the modal structures extracted via POD and DMD revealed different aspects of the flow field, with certain similarities. Liang et al. (2020) used the POD and DMD methods to study the cavitation dynamics in liquid nitrogen cavitation flows, identifying coherent structures and corresponding frequencies. These findings provided valuable guidance for better understanding cavitating flows in practical engineering applications. Han and Tan (2020), after comparing the POD and DMD methods, reported that DMD could accurately decompose the changes in tip leakage vortices in mixed-flow pumps. On the basis of the above studies, it can be concluded that constructing modal decomposition models is an efficient computational mechanism that can effectively manage complex flow fields and identify the primary flow structures (Williams et al., 2015; Taira et al., 2017; Cheng & Chen, 2021).

Although a variety of numerical and experimental methods have been used to investigate hump characteristics under pump operating conditions, the identification of unsteady flow structures and the understanding of the associated instability mechanisms in this region remain limited. In particular, extracting dominant unsteady features and accurately identifying critical vortex structures are challenging. POD and DMD have demonstrated different advantages in analyzing complex flows, and their computational principles are complementary in terms of modal reduction. As a result, the combined use of POD and DMD has become increasingly common in recent studies for extracting and comparing modes in unsteady flow fields (Liu et al., 2019a; Chang & Gao, 2023; Long et al., 2024). On this basis, this study was focused on the typical hump conditions of a reversible pump turbine. LES was employed to obtain transient flow field data, and both POD and DMD were applied to perform modal decomposition. The objectives were to identify energy-dominant flow structures and unstable modes, clarify flow features such as rotating stalls, and provide theoretical guidance for understanding flow mechanisms and improving operational stability.

2. METHODOLOGY

2.1 POD

The goal of POD is to simplify a problem and reduce computational complexity by identifying the most significant modes in the data while reducing the degrees of freedom. The core concept is to begin with a set of spatial data (physical quantities at grid points) arranged in a time sequence and then decompose the fluctuating data via orthogonal decomposition techniques. This process allows for the representation of data as the products of a limited set of orthogonal basis functions and modal coefficients. High-order data are represented via a finite number of basis functions. For example, in the case of transient velocity fields, N transient velocity fields are selected, and the instantaneous velocity is decomposed into a mean value and fluctuating components.

$$u_i(x,t) = \bar{u}_i(x,t) + u_i'(x,t) \tag{1}$$

The time-averaged flow field $\bar{u}_i(x,t)$ is calculated via the velocity field data to represent a flow structure that does not evolve over time. The instantaneous velocity matrix $u_i(x,t)$ that is composed of velocity data at different points in the cross-section is subtracted from the time-averaged flow field matrix $\bar{u}_i(x,t)$, yielding the fluctuating velocity matrix $u_i'(x,t)$ at different time instances. The fluctuating velocity matrix $u_i'(x,t)$ is reconstructed by reducing its dimensionality, and it can be expressed as the product of the first few dominant POD modes $u_j(x)$ and the time-dependent modal coefficients $a_j(t_i)$.

$$u_i'(x,t) = \sum_{j=1}^{N} a_j(t_i) u_j(x) \tag{2}$$

On the basis of the selected N transient velocity fields, a set of fluctuating velocity fields corresponding to N time instances is formed. This process results in a velocity field matrix $U'(x,t)$ that varies over time:

$$U'(x,t) = \begin{bmatrix} u'(x_1,t_1) & \cdots & u'(x_1,t_N) \\ \vdots & \ddots & \vdots \\ u'(x_m,t_1) & \cdots & u'(x_m,t_N) \end{bmatrix} \tag{3}$$

The fluctuating velocity matrix is decomposed into three distinct matrices as follows: $U'(x,t) = BSV^T$. Here, $B \in R^{m\times n}$ is a spatial modal matrix, $S \in R^{n\times n}$ is a rectangular diagonal matrix composed of singular values in descending order, and $V \in R^{n\times n}$ is a constructed modal matrix. The time coefficient is solved as follows: $a = S \cdot V^T$. The energy associated with each mode is calculated by the eigenvalue λ_j: $\lambda_j = S_j^{\,2}$.

The spatial modes $B_j(x)$ obtained through POD and the time coefficients $a_j(t)$ are used to reconstruct the velocity field:

$$U(x,t) = \bar{U}(x,t) + \sum_{j=1}^{N} B_j(x)\, a_j(t) \tag{4}$$

2.2 DMD

DMD decomposes a system along the time dimension to identify dynamic modes, which reflect the inherent frequencies and characteristics of the system. This method is particularly suitable for studying linearized approximations of nonlinear systems, and it can manage high-dimensional time series data. By utilizing the eigenvalues and eigenvectors of a low-dimensional subspace, DMD captures the dominant dynamics of the flow field. The core concept of DMD is to define a spatiotemporal signal U_{tx}, where x represents the data at the signal acquisition points and t represents the changes in the signal over time. The time sampling points are denoted as N, and the number of spatial sampling points is m. The two snapshots v_i and v_{i+1} have a time interval Δt. Under a linear assumption, v_{i+1} can be approximated as Av_i, where $A \in R^{m\times m}$. The DMD algorithm seeks an approximation matrix to replace the high-dimensional matrix A, thereby achieving dimensionality reduction, which can be obtained by performing singular value decomposition (SVD) on v_i.

$$v_i = \begin{bmatrix} u(x_1,t_1) & \cdots & u(x_1,t_{N-1}) \\ \vdots & \ddots & \vdots \\ u(x_m,t_1) & \cdots & u(x_m,t_{N-1}) \end{bmatrix} \tag{5}$$

$$v_{i+1} = \begin{bmatrix} u(x_1,t_2) & \cdots & u(x_1,t_N) \\ \vdots & \ddots & \vdots \\ u(x_m,t_2) & \cdots & u(x_m,t_N) \end{bmatrix} \tag{6}$$

$$v_i = U \Sigma W^T \tag{7}$$

$$U^T A U = U^T v_{i+1} W \Sigma^{-1} = \tilde{A} \tag{8}$$

In the singular value decomposition process described above, $U^T U = I$, and Σ is a diagonal matrix, with its diagonal elements being arranged in descending order. The low-dimensional approximation matrix $\tilde{A}$ is used to closely approximate A. Additionally, the low-dimensional approximation matrix $\tilde{A}$ undergoes eigenvalue decomposition, where the eigenvalues of $\tilde{A}$ are equal to those of A, and the eigenvectors of A are determined by the corresponding modes:

$$\tilde{A} m_i = \lambda_i m_i \tag{9}$$

The DMD modes are defined as follows:

$$q = v_{i+1} W \Sigma^{-1} m \tag{10}$$

The decay rate and frequency of the modal index are represented by the real and imaginary parts of the logarithm of the eigenvalue, respectively:

$$w = \mathrm{Re}\,(\ln(\lambda_i) / \Delta t) \tag{11}$$

$$f = \mathrm{Im}\,(\ln(\lambda_i) / \Delta t) / (2\pi) \tag{12}$$

The initial value matrix b corresponding to the DMD modes is calculated as follows:

$$q \cdot b = v_{x1} \tag{13}$$

Thus, the original flow field is reconstructed, where λ_j^{i-1} represents the Vandermonde matrix storing the variations in the eigenvalues:

$$v_i = \sum_{j=1}^{n} q_j b \lambda_j^{i-1} \tag{14}$$

2.3 Numerical Simulation of Pump Operating Conditions

This study is focused on a specific pump turbine model, which consists of four main components: the spiral casing, guide vane, runner, and draft tube. The key parameters of the model are as follows:

This study is focused on unsteady flow induced by rotating stalls. This flow is characterized by prominent three-dimensional large-scale vortex structures and strong temporal changes. To effectively capture these key flow features, the LES method is employed. Compared with

Table 1 Model parameters

Parameter Name	Parameter Value
Number of Fixed Guide Vanes	20
Number of Variable Guide Vanes	20
Number of Runner Blades	9
Runner Exit Diameter (m)	0.45
Runner Inlet Diameter (m)	0.25
Guide Vane Height (m)	0.04373
Diameter of Guide Vane Distribution Circle (m)	0.54

RANS models, LES provides greater accuracy in resolving unstable modes and transient vortex structures. Although DES combines the advantages of RANS and LES, it often suffers from model switching instability when applied to complex pump turbine flows. Considering the trade-off between accuracy and computational cost, LES is selected as the more appropriate computational approach. The momentum conservation equation based on LES is as follows:

$$\frac{\partial \bar{u}_i}{\partial t}+\frac{\partial\left(\bar{u}_i\bar{u}_j\right)}{\partial x_j}=-\frac{1}{\rho}\frac{\partial \bar{p}}{\partial x_i}+\nu\frac{\partial^2\bar{u}_i}{\partial x_j^2}-\frac{1}{\rho}\frac{\partial\tau_{ij}}{\partial x_j}+f_i,\quad \frac{\partial\bar{u}_i}{\partial x_i}=0 \tag{15}$$

In this equation, τ_{ij} denotes the subgrid-scale stress, and the classical Smagorinsky model is employed in this study (Yang et al., 2012; Heng et al., 2014). Hence, the specific form of the subgrid-scale stress is given by the following equations:

$$\tau_{ij}=\rho\left(\overline{u_i u_j}-\bar{u}_i\bar{u}_j\right) \tag{16}$$

$$\tau_{ij}-\frac{1}{3}\tau_{kk}\delta_{ij}=-2\rho\nu_T\bar{S}_{ij} \tag{17}$$

$$\bar{S}_{ij}=\frac{1}{2}\left(\frac{\partial\bar{u}_i}{\partial x_j}+\frac{\partial\bar{u}_j}{\partial x_i}\right) \tag{18}$$

In this equation, ν_T represents the turbulent viscosity, and its definition is as follows:

$$\nu_T=\left(C_S\Delta\right)^2|\bar{S}| \tag{19}$$

$$|\bar{S}|=\left(2\bar{S}_{ij}\bar{S}_{ij}\right)^{1/2} \tag{20}$$

C_S is a dimensionless parameter that represents the Smagorinsky constant.

Δ is the filter scale, and as Δ approaches zero, it corresponds to direct numerical simulation (DNS).

$|\bar{S}|$ denotes the magnitude of the strain rate tensor.

In this study, five sets of meshes with varying grid densities were used to perform a grid independence test under pump operating conditions. The flow rate was set to 90 kg/s, and the rotational speed was set to 1000 r/min. Structured meshes were generated for all the flow domains of the main components. A pressure inlet boundary condition was applied at the draft tube inlet with a static pressure of 0 Pa, and a mass flow outlet condition of 90 kg/s was set at the outlet of the spiral casing. On the basis of this setup, incompressible flow calculations were carried out via ANSYS–CFX. All the solid walls were treated as no-slip and adiabatic. The interface between the rotating runner and the stationary components, including the guide vane and draft tube, was defined as a sliding interface via the transient rotor–stator model. According to the convergence criteria, the time step was set to 1/360 of a full rotation (Lu et al., 2021; Liang et al., 2024; Xu et al., 2024), i.e., one step per degree of runner rotation, with a sampling frequency of 6000 Hz. The runner completed one full revolution in 0.06 s, corresponding to a rotational frequency (*fn*) of 16.667 Hz. The computed pump head was selected as the evaluation parameter for the grid independence test, as it was a key performance indicator under pump mode and reflected the influence of mesh refinement on pressure loss. The detailed results are shown in Table 2.

Table 2 Mesh information (unit: 10^4 cells)

Mesh ID	Spiral Casing	Guide Vanes	Runner	Draft Tube	Total
1	98	175	201	82	556
2	121	220	276	124	741
3	139	258	356	164	917
4	156	275	446	193	1070
5	195	337	491	213	1236

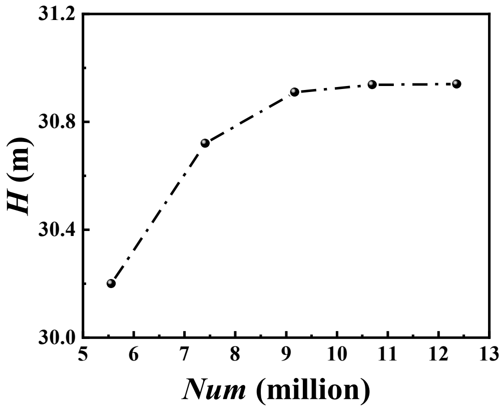

Fig. 2 Grid independence results

The five mesh sets described above were used for simulation to verify grid independence. The corresponding pump head results were used to plot the grid independence curve, as shown in Fig. 2. As the mesh density increased, the calculated head values became more accurate. When the total number of cells reached 10.7 million, the head value tended to stabilize. Considering the overall computational performance, available resources, and the need for subsequent unsteady simulations, this mesh configuration was selected for the final calculations.

2.4 Simulation Verification

On the basis of the simulation results, head and efficiency curves under different flow rates in pump mode were plotted (Dehghan & Shojaeefard, 2022; Dehghan et al., 2024). The numerical data were compared with the experimental results for validation, as shown in Fig. 3 and Fig. 4. The experimental data were obtained from the standard pump turbine model test platform at the Harbin Electric Research Institute, with a measurement uncertainty of ±3%.

As shown in the flow–head characteristic comparison in Fig. 3, the numerical simulation results fit well with the experimental data, and the hump characteristic is clearly captured. The maximum deviation between the simulation and the experimental mean is 4.67%. Before the hump

Table 3 Summary of simulation parameters

Physical Model	Fluid type	Incompressible flow
	Turbulence model	Large eddy simulation (LES)
	Subgrid-scale model (SGS)	Smagorinsky model
Spatial Discretization	Mesh type	Structured mesh
	Number of cells	10.7 million
Temporal Discretization	Time step	1/360 of a rotation period (0.000167 s)
	Total simulation time	30 rotation periods (1.8 s total)
	Sampling frequency	6000 Hz (one sample per degree)
Boundary Conditions	Inlet	Pressure inlet (static pressure: 0 Pa)
	Outlet	Mass flow outlet condition
	Wall boundary	No-slip condition
	Rotating component interface	Transient rotor–stator model, rotational speed: 1000 r/min

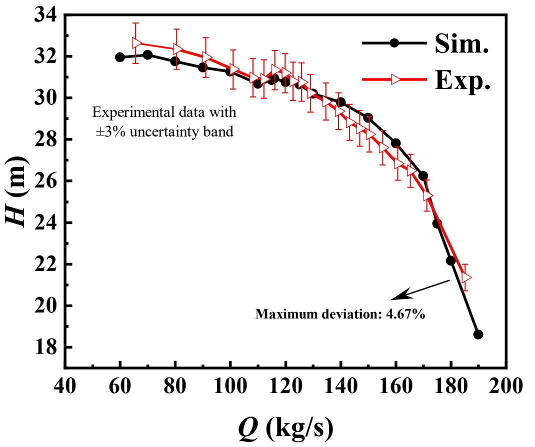

Fig. 3 Flow rate-head comparison curve

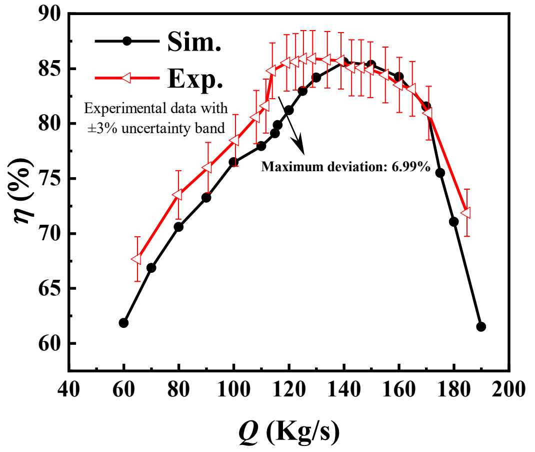

Fig. 4 Flow rate-efficiency comparison curve

region, the simulated head is generally lower than the experimental values. At the lowest point of the hump, the results are closely aligned, whereas at the peak, the simulation slightly underperforms. In Fig. 4, which presents the flow–efficiency characteristic comparison, the simulated efficiency is lower than the experimental results before reaching the peak efficiency point, with a maximum deviation of 6.99%. Notably, within the hump region, the difference in efficiency is more pronounced. The experimental efficiency approaches its peak, whereas the simulated efficiency is still increasing. As the flow rate continues to increase, the gap between the simulated and experimental results gradually narrows. This discrepancy is attributed to complex unsteady phenomena in the hump region, such as strong backflow, flow separation, and rotating stall, which are difficult to capture accurately in simulations. These effects lead to an overestimation of hydraulic losses, resulting in a lower prediction efficiency than that of experimental measurements. Overall, the simulation performs well in capturing the hump characteristics, confirming the reliability of the numerical approach. The key simulation parameters are summarized in Table 3 and serve as a basis for further calculations under various pump operating conditions.

3. RESULTS AND DISCUSSION

3.1 Hydraulic Losses Under Different Flow Conditions

The head is a key indicator of the operating performance of a pump turbine, and it represents the height to which the pump can lift water. Since the head is significantly affected by flow loss, the total pressure drop across each flow passage component is used under different flow conditions to characterize the energy variations. The total pressure drop is calculated on the basis of the inlet and outlet cross-sections of each numerical domain, including the spiral casing, guide vane, runner, and draft tube. These cross-sections correspond to the boundaries of each flow region. The resulting data describe the performance of the pump turbine in pump mode, including the pressure loss curves of each component and the proportion of total pressure loss attributed to each region.

According to the pressure loss–flow rate curves for each flow domain shown in Fig. 5 and Fig. 6, the losses in different domains are different under low-flow conditions, with the losses being primarily concentrated in the guide vane and runner regions. The presence of blades and the dynamic–static interference in these regions cause complex phenomena, such as vortices, leading to significant energy losses. As the flow rate increases, the fluid gradually fills the entire passage, and the influences of the solid components on the liquid flow diminish. Under high-flow conditions, the overall loss increases, mainly occurring in the spiral casing region. The energy

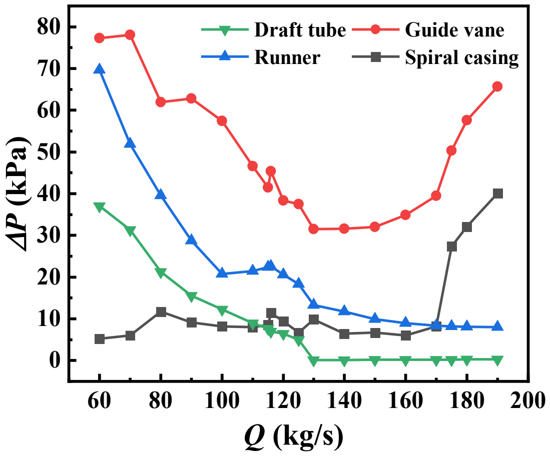

Fig. 5 Pressure loss curves for flow domains

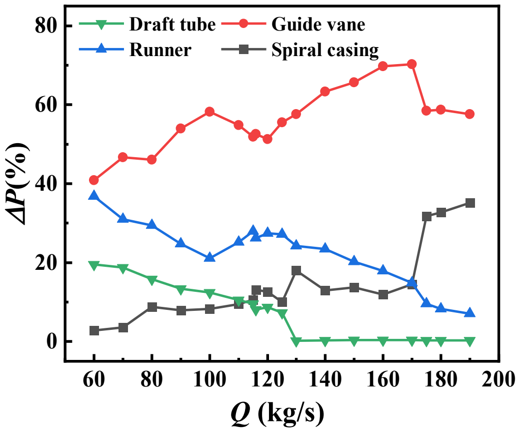

Fig. 6 Pressure loss proportions for flow domains

loss variation is consistent with the characteristics of the efficiency curve as the flow rate increases. Notably, in the hump region, the losses in both the guide vane and runner regions slightly increase. This phenomenon is closely related to the unstable flow in the hump region, particularly the flow separation in the guide vane region, the vortices and recirculation in the runner region, and the dynamic–static interference in the blade-free region between these two areas.

On the basis of the external characteristic performance described above, four flow conditions are selected for in-depth analysis of the internal flow field changes in the guide vane and rotor domains: the prehump condition at 90 kg/s, the lowest point of the hump at 110 kg/s, the highest point of the hump at 116 kg/s, and the optimal efficiency condition at 140 kg/s. This analysis aims to further investigate flow evolution characteristics with varying flow rates, thereby providing a better understanding of the energy loss mechanisms during pump operation and the formation of the hump region.

3.2 Analysis of Guide Vane Flow Domain Characteristics

The guide vane region is often closely associated with flow separation, vortex, and other complex flow phenomena. Among all the energy losses in the flow components, the losses in the guide vane region account for the highest proportion. According to the streamline distribution shown in Fig. 7, under different flow conditions, the flow passage is filled with vortices of varying sizes. When the flow rate is 90 kg/s, the fluid flows smoothly, and large vortices break down into smaller vortices, reducing flow losses and increasing efficiency. In the hump region, large vortices and significant flow separation occur between the fixed guide vanes, leading to blockage in the passage. The flow within the circumferential guide vane region becomes highly uneven, and the losses increase slightly. As the flow rate approaches the highest point of the hump (116 kg/s), the flow field gradually deteriorates. However, at the optimal efficiency point, the vortices in the flow passage are significantly reduced, and the streamlines become smooth, resulting in the lowest flow losses.

On the basis of the streamline distribution shown in the previous section, the flow between the passages varies under different flow conditions, although vortex and flow separation phenomena are generally present. These

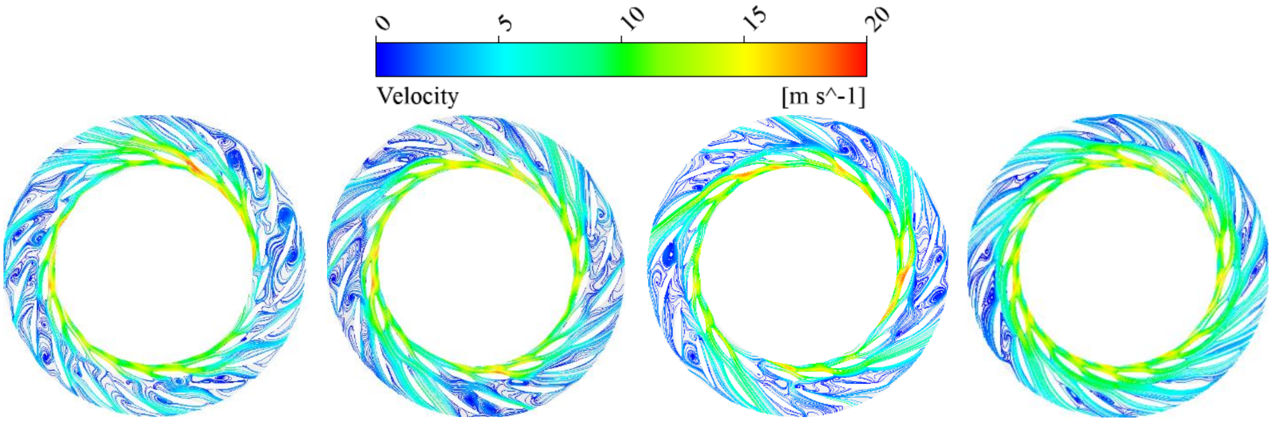

(a) *Q* 90 kg/s (b) *Q* 110 kg/s (c) *Q* 116 kg/s (d) *Q* 140 kg/s

Fig. 7 Streamline distribution on the mid-section of the guide vane region

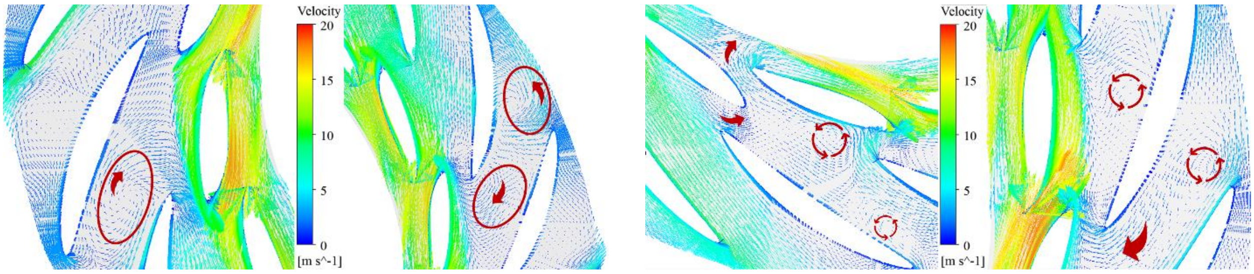

(a) *Q* 110 kg/s (b) *Q* 116 kg/s

Fig. 8 Velocity vector plots of the mid-sections of the guide vane regions in the hump region

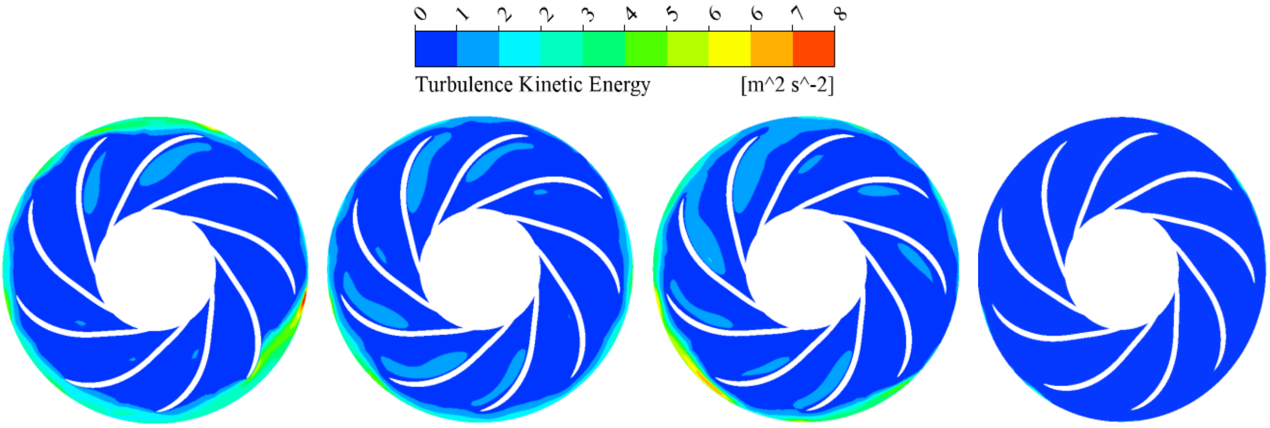

(a) *Q* 90 kg/s (b) *Q* 110 kg/s (c) *Q* 116 kg/s (d) *Q* 140 kg/s

Fig. 9 Distributions of turbulent kinetic energies on the planes of the runner blades

phenomena become particularly pronounced in the hump region, where the flow in most of the passages is blocked, and uneven flow patterns appear in the circumferential direction. To further investigate this characteristic, vector plots are used to describe the detailed flow characteristics of the guide vane domain during the hump period. These characteristics are then combined with the streamline distribution to analyze the flow instability under flow conditions of 110 kg/s and 116 kg/s.

On the basis of the velocity vector plot of the guide vane region in Fig. 8, in the hump region, the passages are filled with pronounced vortex and recirculation flows. As the fluid exits the runner, flow separation occurs at the trailing edges of the variable guide vanes, and high-speed flow is observed beneath the vane until it reaches the next variable guide vane, where it merges with the mainstream flow. The instability in the guide vane region can be approximately divided into two parts. First, vortex backflow occurs, where fluid moves toward the runner outlet and disrupts the normal flow structure. Second, part of the outflow from the runner passes through the region between the leading edge of the variable guide vane and the trailing edge of the fixed guide vane. In this area, the reduced flow passage causes an increase in velocity. In addition, obvious boundary layer separation appears along the upper surface of the fixed guide vane, resulting in vortex formation between adjacent vanes. This phenomenon disturbs the original flow and alters the behavior of the flow near the lower surface. These unsteady phenomena lead to a highly disordered flow field and further confirm the strong correlation with the flow instability observed in the hump region.

3.3 Analysis of the Runner Flow Domain Characteristics

The runner, which is akin to the "heart" of a pump, plays a critical role in its operation. The runner draws water from the draft tube while converting the rotational mechanical energy into fluid kinetic energy, facilitating energy input. Owing to the spatial distortion of the runner blades, significant energy losses can occur as the fluid flows through them. Moreover, these losses vary with changes in the flow rate. Therefore, a detailed analysis of the flow characteristics is conducted via the turbulent kinetic energy distribution shown in Fig. 9.

On the basis of the loss curve, the flow loss in the runner region ranks second only to the guide vane region in the early stages of the flow component loss process. At a flow rate of 90 kg/s, a small-scale turbulent distribution appears within the runner passages; the level of instability decreases at the runner outlet as the flow rate increases. Starting at 110 kg/s, the flow field characteristics shift, with large, irregular regions of turbulent kinetic energy forming within the runner blade passages attached to the suction side. Additionally, flow deterioration at the runner outlet begins to intensify, indicating that the turbulence distributions and vortices in the passages are key factors affecting flow instability in the hump region. As the flow rate increases further, at 140 kg/s, the turbulent kinetic energy distribution becomes less pronounced, indicating

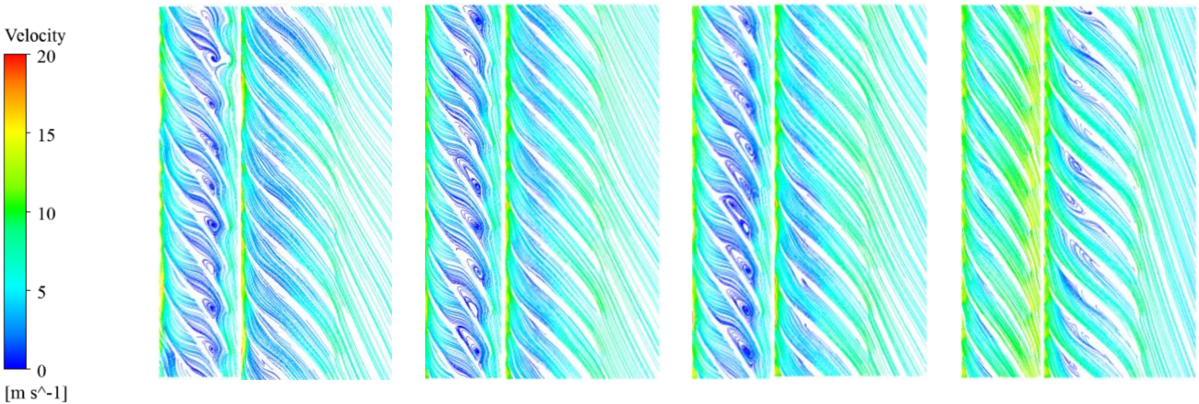

(a) *Q* 90 kg/s (b) *Q* 110 kg/s (c) *Q* 116 kg/s (d) *Q* 140 kg/s

Fig. 10 Characteristics of the planar velocity fields on the runner blades (left: span 0.9; right: span 0.5)

that the flow loss between the passages is minimal, which aligns with the trend observed in the pressure loss curve of the runner region.

To better describe the flow variations between the runner blades, the flow patterns are further illustrated via a streamline distribution, as shown in Fig. 10. The diagram on the left corresponds to a span of 0.9, which is near the runner's shroud, whereas the diagram on the right corresponds to a span of 0.5, representing the area near the middle of the hub and shroud. At a span of 0.9, a noticeable vortex is observed near the shroud. In contrast, the flow between the blades near a span of 0.5 remains more stable. When the flow enters the hump region, large vortices begin to develop near the shroud, occupying almost the entire passage along the suction side of the blade, which reduces the flow area. This phenomenon occurs at the mid-span, where flow instability starts to emerge. As the flow rate increases further, the vortices near the shroud disappear, and the flow lines become smooth and continuous, indicating an improvement in the flow conditions. With increasing flow rate, only small-scale vortex fluctuations appear at the mid-span, and the overall loss in the runner region significantly decreases.

3.4 Analysis of Flow Dynamics in the Hump Region

Overall, the vortex generated by flow separation between blade passages and the disturbed flow at the runner inlet are closely related to the flow instability in the hump region. On the basis of the flow characteristics under different operating conditions, the initial condition of 110 kg/s in the hump region is selected for detailed analysis. Considering the mid-span section as an example, the formation of the hump phenomenon and its relationship with flow instability are further investigated.

As shown in Fig. 11, the velocity distribution in the XY cross-section of the pump indicates that within one rotational cycle, the flow consistently enters from the runner inlet and exits through the spiral casing after passing through the runner. The flow within the runner is concentrated in the middle region of the blade passage. A low-velocity region is observed on the pressure side of the blades, which is caused by flow separation due to blade rotation, leading to the formation of vortices that disturb the mainstream flow and move upward along the blade surface. On the suction side, the flow is influenced by the vortex and adheres to the suction surface, accelerating under the action of blades. When the fluid reaches the runner outlet, the flow cross-sectional area suddenly increases. As the blades rotate, the fluid on the suction side cannot maintain its original motion, resulting in flow separation near the outlet. At this point, complex vortex flows exist on both sides of the blades, forcing the mainstream flow to remain in the middle of the blade passage until a certain velocity water ring is formed in the blade-free region. As the rotational cycle progresses, the flow within the runner region remains relatively similar.

In the blade-free region and guide vane region, significantly nonuniform flow occurs, with local flow velocities decreasing and reverse flow emerging. These unstable vortices, in combination with the pump rotational direction, result in periodic flow instability and clear rotational stall characteristics. At the runner outlet side, the fluid converges on both sides of the blades. Owing to the narrow space in the blade-free region and the limited flow passage in the variable guide vane region, some of the fluid accelerates through. Conversely, another portion of the fluid continues undergoing circular motion, merging with the flow from other outlet regions. This process creates complex flow in the area. Owing to uneven pressure distribution, the fluid is prone to separation, resulting in a decrease in velocity or even reverse flow. As the fluid enters the guide vane region, it is affected by the guide vanes, leading to dynamic–static interference, which causes flow separation and generates vortices in the passage, thereby hindering normal flow and further exacerbating flow nonuniformity. Over time, the velocity distribution within the guide vane passage changes, with the vortex states continuously shifting and the positions of the stall characteristics varying accordingly.

In the above analysis, the complex flow characteristics in the guide vane region are closely related to the formation of the hump phenomenon. Therefore, the flow characteristics in this region are illustrated via the streamline distribution at the cross-section shown in Fig. 12. This section includes the blade-free region, variable guide vanes, fixed guide vanes, and the external flow region of the guide vanes.

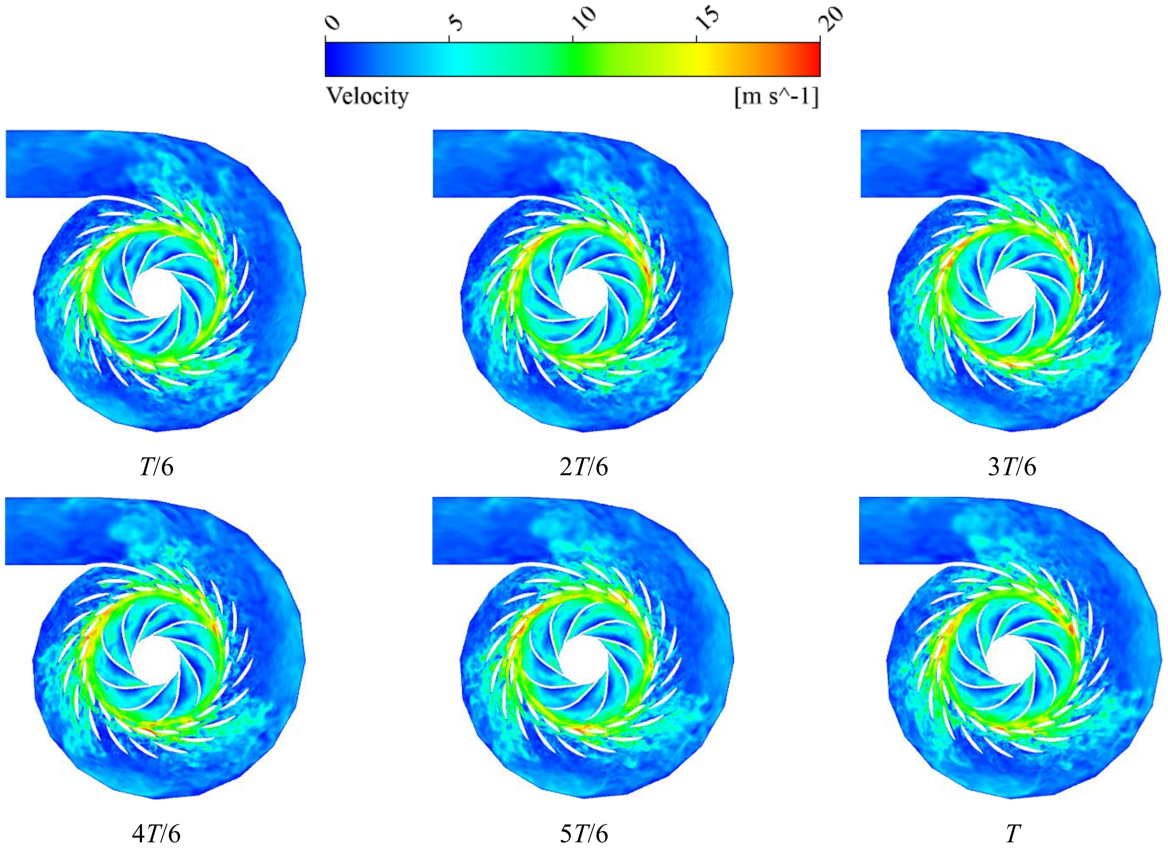

T/6 2*T*/6 3*T*/6

4*T*/6 5*T*/6 *T*

Fig. 11 Velocity distributions at different time instances in the pump plane

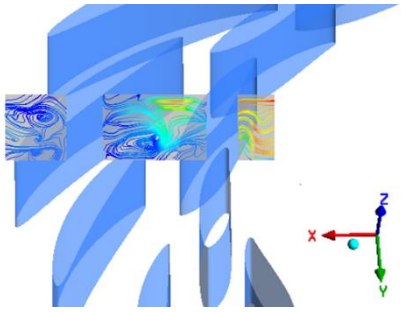

Fig. 12 Schematic diagram of the guide vane region cross-section

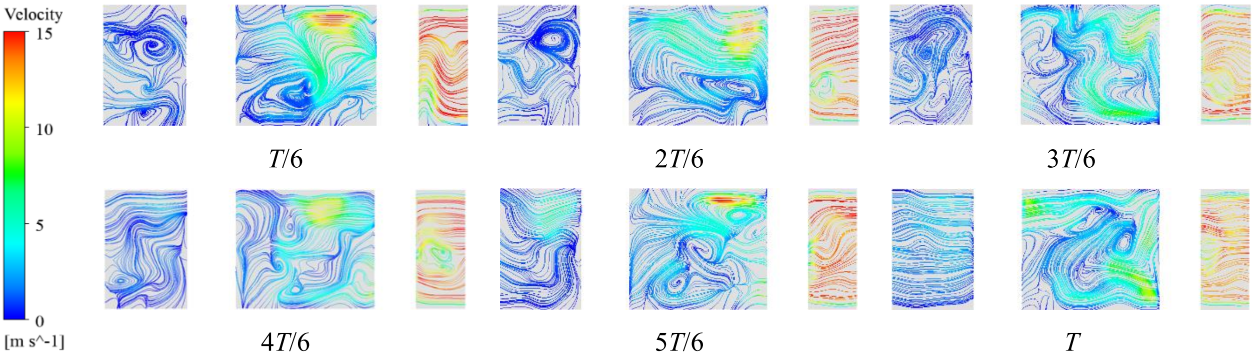

T/6 2*T*/6 3*T*/6

4*T*/6 5*T*/6 *T*

Fig. 13 Streamline distributions in the guide vane region

As shown in Fig. 13, the streamline distribution in the guide vane region indicates that the flow velocity is greater near the blade-free region. Flow fluctuations occur near the shroud, and over time, vortices gradually form, disturbing the flow fields on both sides. Within the guide vane region, the flow becomes chaotic, particularly in the

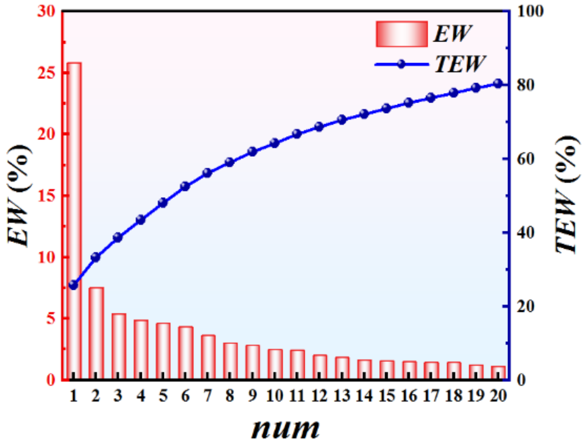

Fig. 14 Energy distributions of the first 20 POD modes

upper half, where the velocity is relatively high. Simultaneously, the overall flow velocity decreases, and it is accompanied by disordered vortex flow, severely disrupting mainstream movement. Vortex phenomena are clearly evident in the streamline diagram, suggesting that flow separation is likely to occur near the guide vanes. Over time, the single large vortex near the shroud expands upward toward the hub and transforms into multiple irregular vortices, inducing complex motion. As the fluid exits the guide vane region, the flow velocity significantly decreases, indicating that this region is not the main outlet area and that the complex vortices gradually evolve into steady streamlines.

3.5 Flow Field POD Analysis

The time-resolved flow field data under pump operating conditions are analyzed via modal decomposition. The original flow field is considered a superposition of modal structures on the mean field. On the basis of the characteristics of each mode, dominant flow structures can be identified, allowing further insight into the causes of flow instability. Figure 14 presents the energy weight (EW) of the first 20 POD modes at the mid-span section, along with their total energy weight (TEW). The results show that the first mode has the highest energy, which is followed by gradual declines in the energies of high modes. Except for the significant decrease from the first mode to the second mode, the differences between the subsequent modes are small, indicating that a slow decay occurs. As the number of modes increases, the energy curve flattens, and the cumulative energy of the first 20 modes accounts for approximately 80% of the total energy. This result suggests that multiple dominant structures exist in the pump flow field, indicating that complex flow behavior is likely related to large-scale vortical features in the system.

On the basis of the energy distribution characteristics, the top 10 POD modes with the highest energy are selected for further analysis. Their typical flow structures are shown in Fig. 15. The first three modes contribute significantly to the total energy and clearly capture the dominant flow features in the guide vane region, indicating that this area plays a leading role in the overall unsteady flow. The interaction between the variable guide vane and the runner introduces noticeable flow nonuniformity. In the mode shapes, this nonuniformity appears as strong alternating positive and negative regions between guide vanes, reflecting the coupled evolution of flow separation and vortex structures. This finding indicates that the guide vane area is a primary source of unsteady disturbances.

The 4th and 5th POD modes are mainly concentrated in the bladeless region at the runner outlet, where the velocity field shows periodic alternating patterns. This phenomenon reflects unsteady pulsation behavior induced by dynamic–static interference due to runner rotation. These modal structures are closely associated with local rotating stall and flow instability. As shown in Fig. 8, this region is prone to flow separation, leading to the formation of two coherent disturbance structures in the mode field. As the mode number increases, the modal scale in the

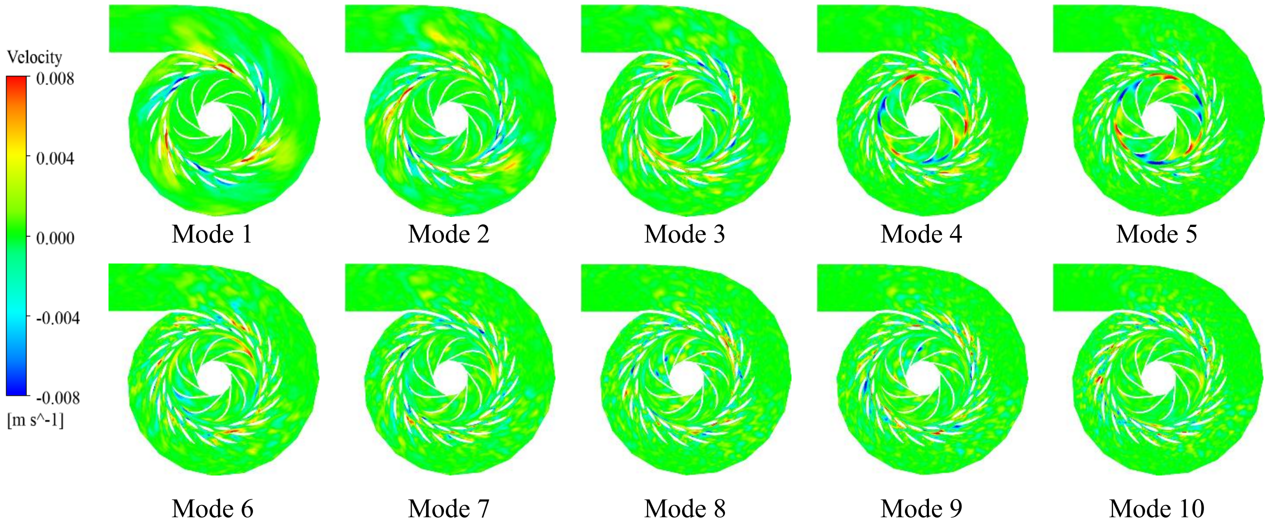

Mode 1 Mode 2 Mode 3 Mode 4 Mode 5

Mode 6 Mode 7 Mode 8 Mode 9 Mode 10

Fig. 15 Velocity field characteristics of the first 10 POD modes

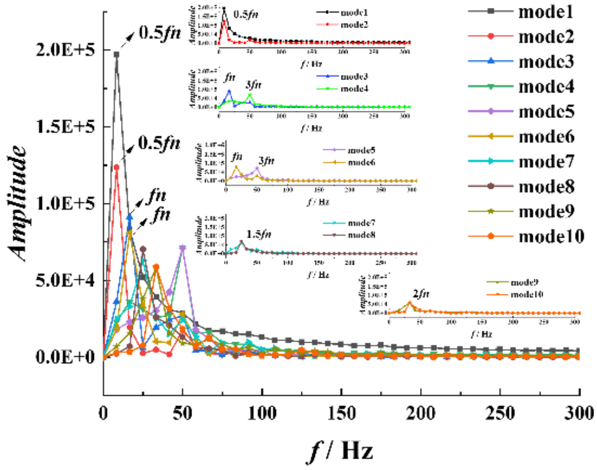

Fig. 16 Frequency spectra of time coefficients for the first 10 POD modes

guide vane region decreases, and the energy contribution rapidly decreases, indicating that high-order modes mainly represent small-scale disturbances. However, some mid-to-high-order modes still exhibit alternating positive and negative structures along the suction side within the runner passages, suggesting the persistent effect of flow separation in this region.

Figure 16 presents the frequency spectra of the temporal coefficients corresponding to the first 10 POD modes. The modes appear in pairs with the same dominant frequency, indicating spatial development of the same vortex structure. On the plane where the runner and guide vane coexist, the dominant frequency of the 1st and 2nd modes is close to 0.5 *fn*, which is in the low-frequency range and the main flow behavior associated with low-frequency vortex structures in the guide vane region. The 3rd mode has a dominant frequency of *fn*, corresponding to the rotational frequency and indicating that the flow structures are dominated by the runner. The 4th and 5th modes have a dominant frequency of approximately 3 *fn*, which reflects the rotating stall caused by dynamic–static interference in the bladeless region. As the mode number increases, the dominant frequency changes, and the flow behavior increases in complexity. Since POD ranks modes by energy (eigenvalue), a few modes can capture the main spatial features of the flow, indicating their relative contributions to the overall flow structure.

To better understand the flow structures associated with the hump characteristics, the flow fields in the guide vane and runner regions are analyzed separately. The velocity field features of the 1st to 10th POD modes in the guide vane region are presented in Fig. 17. In the 1st to 5th modes, various disturbances are observed, which are generally characterized by alternating positive and negative flow structures on both sides of the vanes. The presence of guide vanes alters the flow direction and velocity distribution, resulting in more pronounced pulsations. These dynamic changes are likely related to the complex interactions between the guide vanes and flow, leading to spatially nonuniform modal patterns. In the 6th to 10th modes, the flow is concentrated mainly between the fixed and variable guide vanes, forming alternating coherent structures. Significant flow separation and vortex pulsations appear between flow passages, along with pronounced circumferential nonuniformity. These rotating stall characteristics in the guide vane region represent key features in the sectional modal patterns and are a major contributor to flow instability.

Figure 18 shows the velocity field features of the 1st to 10th POD modes in the runner region. In particular, the 1st and 2nd modes clearly exhibit periodic alternations of positive and negative structures at the runner outlet that are closely related to dynamic–static interference. These structures show strong spatial continuity and dominate the distribution of unsteady energy. The vortex motion near the outlet affects the outflow and interferes with the normal flow in the bladeless region, potentially leading to operational instability. The 3rd and 4th modes capture the main flow features between runner passages, representing secondary large-scale structures associated with rotor

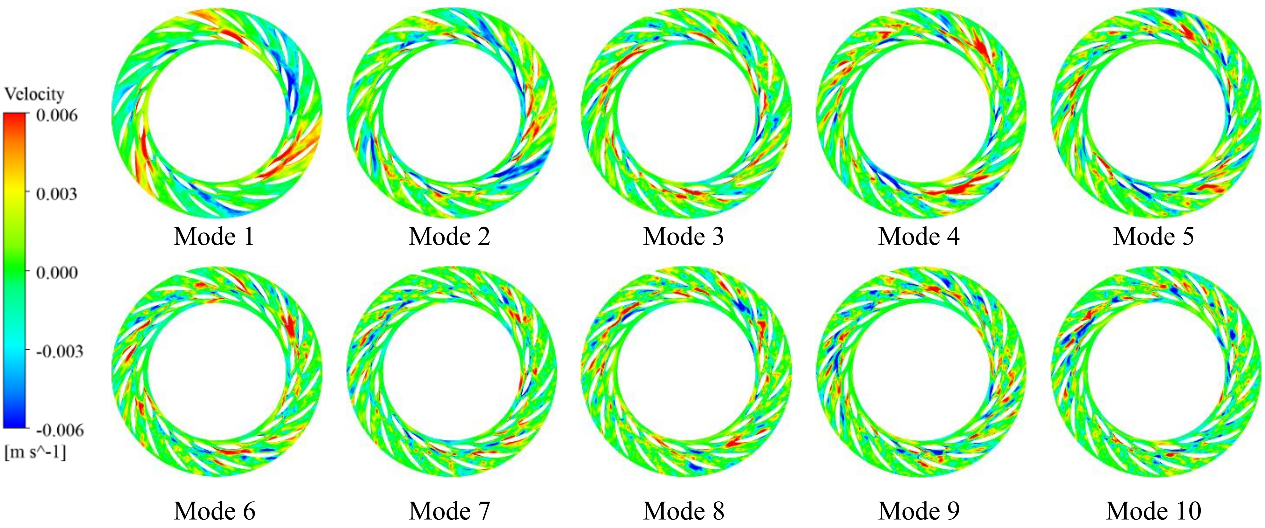

Mode 1 Mode 2 Mode 3 Mode 4 Mode 5
Mode 6 Mode 7 Mode 8 Mode 9 Mode 10

Fig. 17 Velocity field characteristics of the first 10 POD modes in the guide vane region

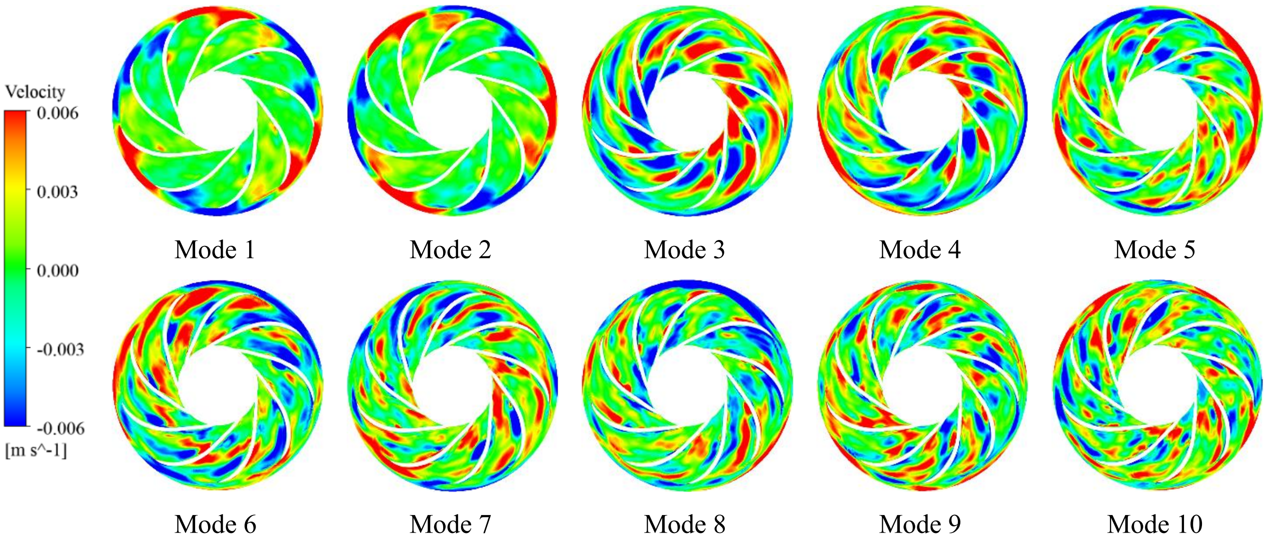

Fig. 18 Velocity field characteristics of the first 10 POD modes in the runner region

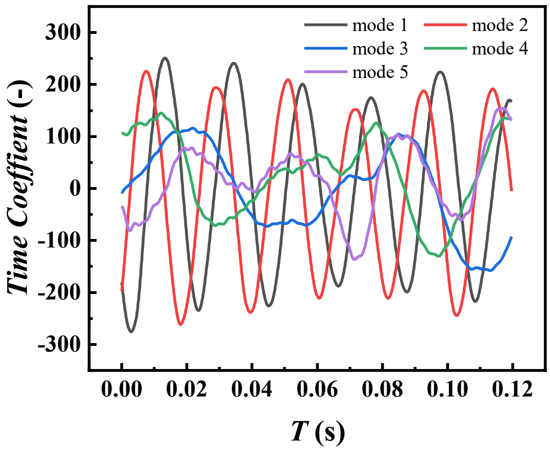

Fig. 19 Time coefficients of the first 5 POD modes in the runner region

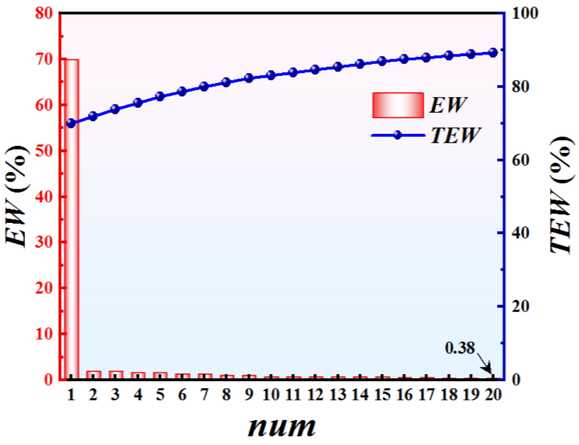

Fig. 20 Energy distributions of the first 20 DMD modes

motion. Alternating structures remain distinct, and the interference patterns between passages appear symmetric. As the mode number increases, the flow features between passages increase in complexity, with local interference and separation becoming more pronounced. Unsteady pulsations are intensified because of the influences of both runner rotation and main flow structures. Within the runner channels, coherent positive–negative structures tend to form along the suction sides of the blades, continuously interacting and asymmetrically developing. These observations suggest that the low-order modes correspond to specific flow mechanisms, such as rotating stall and dynamic–static interference phenomena, whereas the high-order modes capture mainly small-scale vortex motions.

On the basis of the modal characteristics in the runner region, the temporal coefficients of the 1st to 5th POD modes shown in Fig. 19 are further analyzed. The results reveal that the 1st and 2nd modes clearly exhibit sinusoidal fluctuations, which is consistent with the periodic alternations of positive and negative structures at the runner outlet. This phenomenon confirms the flow features associated with dynamic–static interference in the bladeless region. The 3rd and 4th modes each have fluctuation periods of approximately 0.06 s, which matches the rotational period of the runner. These modes together represent the dominant circumferentially propagating flow structures and characterize the main features of rotating flow within the runner. The 5th mode exhibits a fluctuation period close to half of the rotational period, corresponding to twice the rotational frequency. This phenomenon reflects the high-frequency unsteady behavior in the runner flow field, which is associated with the turbulence and evolution of fine-scale vortices between blade passages.

Insights into the physical definitions of the modes help reveal the contributions of flow features at different scales in complex flows and their spatial representations in the POD mode.

3.6 Flow Field DMD Analysis

The transient data obtained under hump conditions are processed via DMD. Similar to POD, the DMD modes are ranked by energy content. As shown in Fig. 20, the

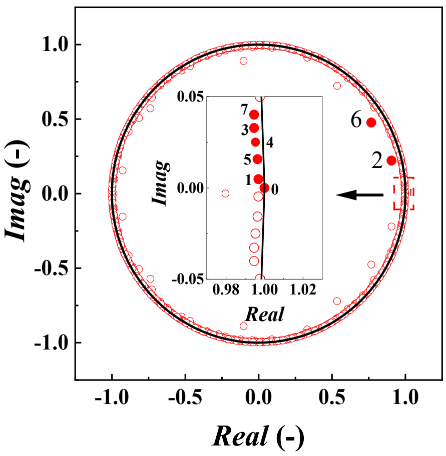

Fig. 21 Distributions of eigenvalues

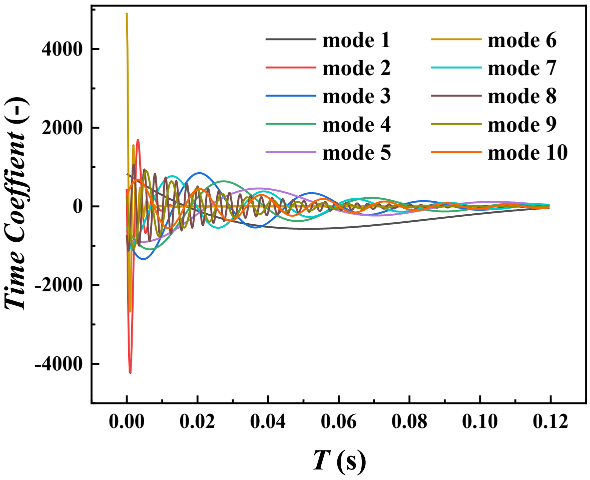

Fig. 22 Time coefficients of the first 10 DMD modes

energy contribution of each mode decreases with increasing mode number, exhibiting a relatively steep decline. Unlike POD, the first DMD mode has a significantly larger energy share, indicating a much greater influence on the overall flow structure. This dominant mode represents the time-averaged component of the flow field and is referred to as the 0th mode. According to the cumulative energy curve, the first 20 modes account for nearly 90% of the total energy. Therefore, analyzing the flow characteristics of the leading modes can help identify dominant flow structures and determine instability sources.

Figure 21 shows the distributions of DMD eigenvalues, which are plotted in the complex plane with the real part on the horizontal axis and the imaginary part on the vertical axis. A unit circle is included as a reference. All the eigenvalues lie on or within the unit circle, indicating good modal stability. The eigenvalues exhibit conjugate symmetry about the imaginary axis, indicating that each pair has imaginary parts of equal magnitude and opposite sign. These phenomena correspond to conjugate modes that represent the same flow structure. Notably, the 0th mode, which has the highest energy contribution, has an eigenvalue located exactly on the unit circle with a frequency of zero, indicating that it is a time-invariant mean-flow mode. This finding is consistent with the energy distribution shown in Fig. 20 and further confirms its dominant role in the overall flow structure.

Figure 22 presents the temporal changes in the time coefficients corresponding to the first 10 DMD modes. The trends show that the energy-ranked modes contribute primarily in the early stage, where the coefficients exhibit periodic fluctuations before gradually decreasing and stabilizing. This finding indicates that the influence of each mode varies over time and is closely related to the modal composition of the flow field at a given moment. By analyzing the behaviors of the time coefficients, the temporal importance of individual modes can be assessed, allowing targeted investigation of specific modal features and quick identification of possible sources of flow instability.

On the basis of the energy distribution of the DMD modes, the flow structures of the first 10 modes at the mid-span section are analyzed, as shown in Fig. 23. The 1st DMD mode mainly reflects flow nonuniformity in the guide vane region, similar to the 1st POD mode. This phenomenon indicates that unsteady disturbances in this region play dominant roles in the overall flow and are key sources of system instability. The 2nd mode highlights the vortex structures between the variable and fixed guide vanes, showing a clear pattern of alternating positive and negative disturbances. This finding reveals strong shear effects and vortex dynamics within that area.

As the mode number increases, the DMD modes exhibit stronger periodic alternating features in the guide vane region, whereas localized pulsation clusters gradually appear near the suction sides of the runner blades. This phenomenon reflects the spatial expansion of disturbance structures. In particular, the 8th mode reveals a disturbance pattern consistent with the POD results: the velocity field in the bladeless region clearly alternates between positive and negative distributions, displaying a typical periodic structure. The relative motion between the runner and guide vane induces periodic disturbances that trigger unsteady flow behavior. This result leads to the alternating dominance of velocity components in the bladeless region, forming two coherent structures that alternate in time. This pattern reflects a typical rotating stall phenomenon and further confirms the flow instability in this region. Notably, the coherent structures identified via DMD are smaller in scale than those identified via POD are, indicating the superior spatiotemporal resolution capabilities of DMD.

Overall, DMD provides more detailed insight into the specific disturbance structures of each mode, with clear advantages in capturing dynamic features. In contrast, POD focuses on extracting dominant structures on the basis of energy contribution, often combines multiple flow characteristics and is highly suitable for representing the overall spatial distribution. The two methods show good consistency in identifying major disturbance structures in the guide vane region. However, DMD demonstrates relatively high sensitivity and clarity in revealing rotating stall and periodic unsteady behaviors. Therefore,

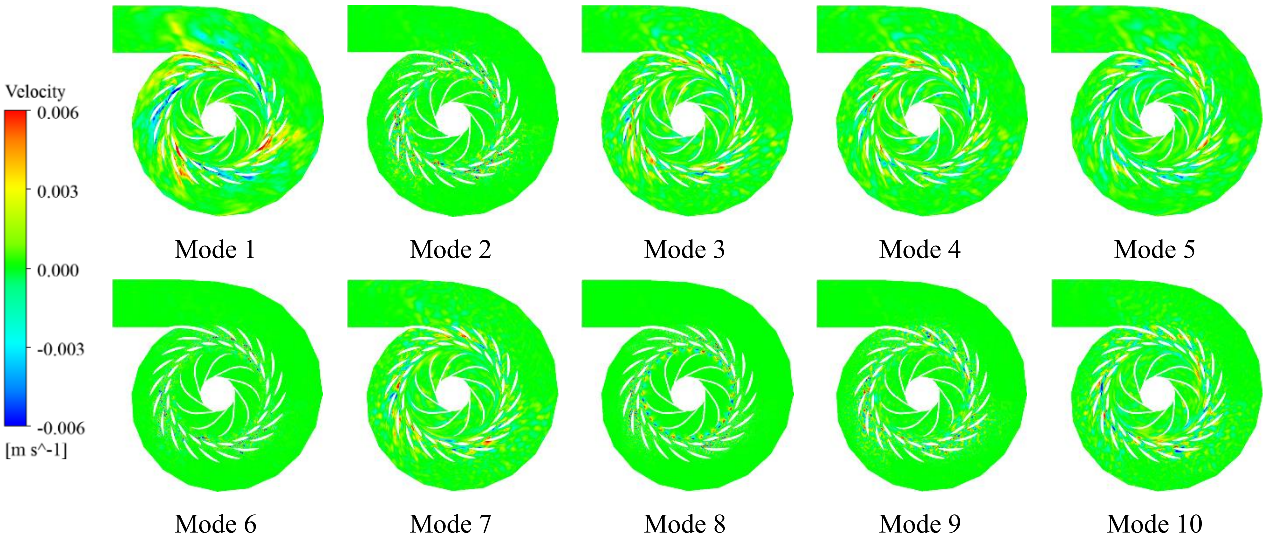

Fig. 23 Velocity field characteristics of the first 10 DMD modes

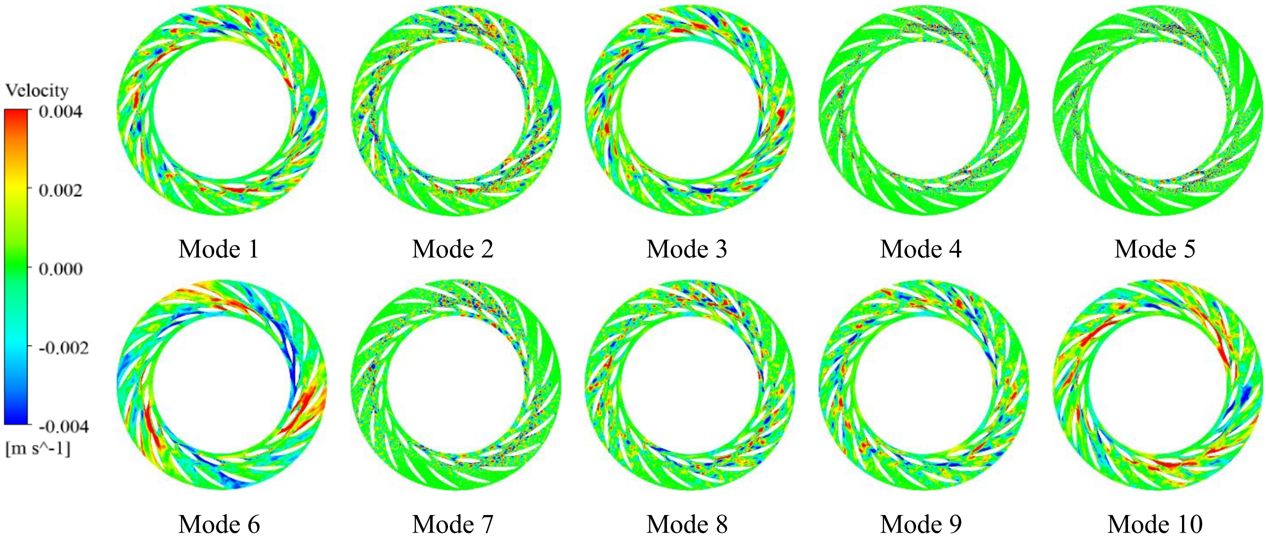

Fig. 24 Velocity field characteristics of the first 10 DMD modes in the guide vane region

combining modal analysis via both POD and DMD allows not only the identification of dominant flow structures from a spatial energy perspective but also a comprehensive understanding of flow instability from the perspective of temporal evolution. This result provides a comprehensive and reliable theoretical basis for analyzing and controlling complex internal flow fields.

On the basis of the above analysis, the modal characteristics of the guide vane and runner regions are further examined. Figure 24 shows the velocity fields of the first 10 DMD modes in the guide vane region. The results indicate that both DMD and POD effectively capture the rotating stall structures in this region and exhibit similar modal features. However, the interference structures in the DMD modes are smaller in scale and more localized. These disturbances are mainly concentrated between the fixed and variable guide vanes and near the guide vane inlet. This result suggests that the presence of guide vanes tends to induce flow separation, leading to the formation of complex vortex structures. These small-scale vortices interfere with the main flow and increase hydraulic losses, which in turn contribute to operational instability.

Figure 25 shows the velocity field features of the first 10 DMD modes in the runner region. These modes reveal not only unsteady disturbances between blade passages but also clear periodic alternating structures in the bladeless region caused by the rotating stall phenomenon, which is characterized by alternating positive and negative disturbances that lead to flow disorder. The 1st mode reflects strong unsteady behavior within the runner passages and has a high energy contribution, indicating its dominant role in the flow. The 2nd mode closely matches the first two POD modes, which represent the same flow structure and clearly capture the rotating stall induced by dynamic–static interference at the runner outlet. As the mode number increases, small-scale unsteady features emerge, and these disturbances significantly interfere with the flow, contributing to instability. The 8th DMD mode corresponds to the 5th POD mode and reflects turbulence

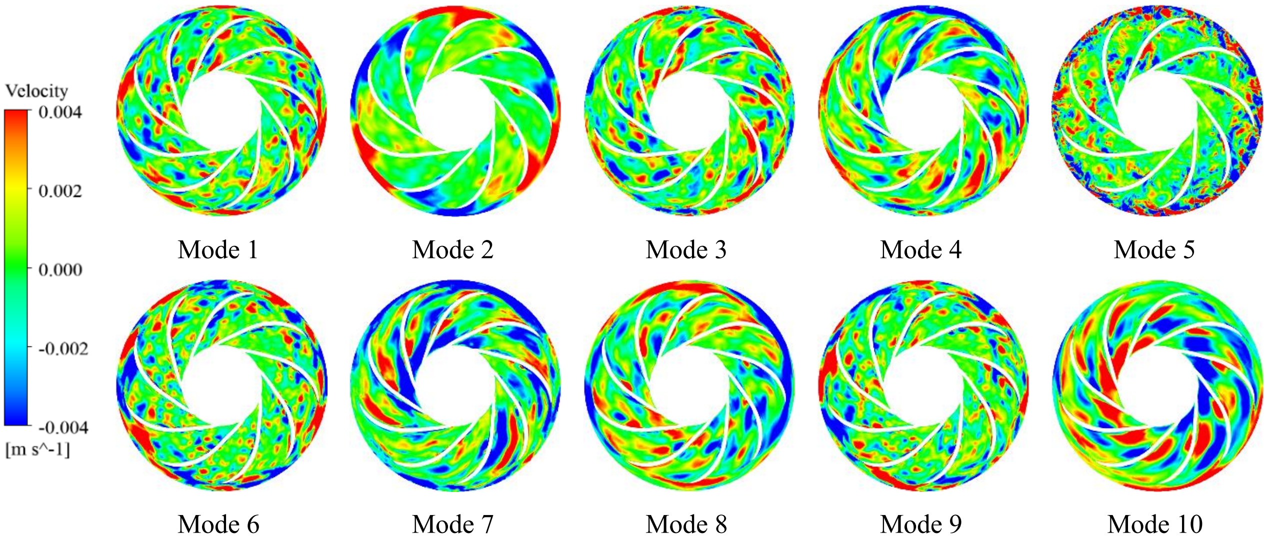

Fig. 25 Velocity field characteristics of the first 10 DMD modes in the runner region

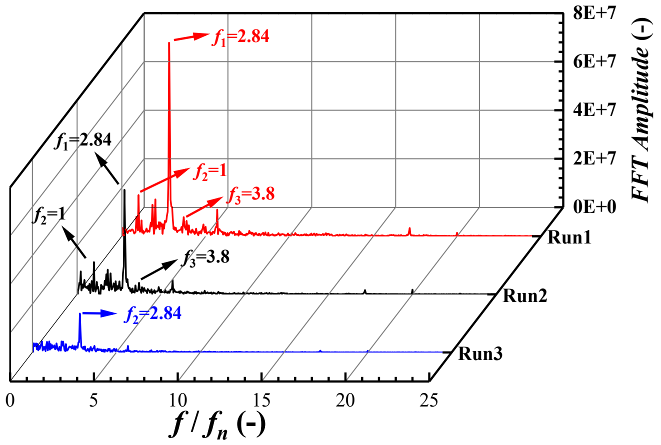

Fig. 26 Pressure spectra at monitoring points in the runner region

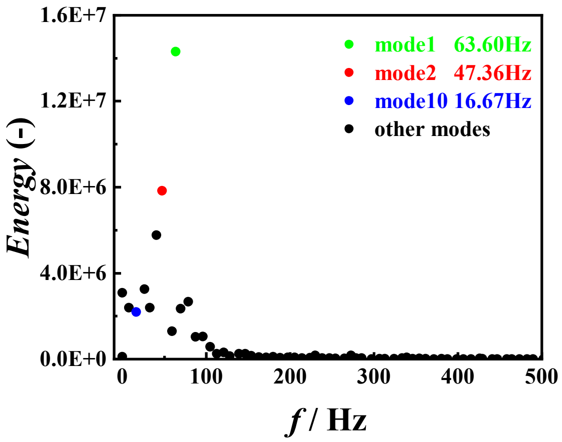

Fig. 27 Energy spectra of DMD modes in the runner region

and small vortex structures between blade passages. Notably, the 10th DMD mode begins to show flow characteristics similar to those of the 3rd and 4th POD modes, which is indicative of the rotating flow structure of the runner. These results further confirm that the low-order modes in the DMD capture the key features associated with flow instability.

To further characterize the flow behavior in the runner region, Fig. 26 and Fig. 27 present the pressure spectra at monitoring points and the corresponding DMD mode energy spectra. The monitoring points are arranged sequentially from the runner inlet to the outlet. By comparing the dominant frequencies from the pressure spectra with those from the DMD modes, unsteady structures in the flow field can be identified more accurately. The runner rotational frequency is 16.667 Hz. At all three monitoring points, the dominant pressure frequency is 2.84 *fn*, which corresponds to the 2nd DMD mode. This mode represents the rotating stall caused by dynamic–static interference near the runner outlet. This finding is consistent with the POD result, which reveals a similar structure close to 3 *fn*. Owing to the limited number of time snapshots used in POD, the temporal resolution is relatively low, making DMD more effective in capturing frequency-specific features. DMD provides precise identification of instability-related structures and combining it with POD further enhances the understanding of the rotating stall mechanism induced by dynamic–static interference. In addition, the frequency of the 1st DMD mode matches the third dominant pressure frequency ($f_3 \approx 3.8\ fn$), indicating a dominant unsteady disturbance within the runner passages. As previously noted, the 10th DMD mode corresponds to the 3rd and 4th POD modes and matches the runner rotational frequency, reflecting the dominant rotating structure inside the runner. Other modes contribute varying degrees of disturbance at their respective frequencies, collectively shaping the flow instability. This analysis effectively reveals the relationships between the frequency contents and flow mechanisms, improving the understanding of complex unsteady flow behaviors and confirming that the low-order modes play key roles in driving flow instability.

3.7 Complementarity of POD and DMD

In summary, a systematic analysis of the first 10 POD and DMD modes in both the guide vane and runner regions reveals that each method offers distinct advantages in capturing unsteady flow behavior under hump conditions. The POD method is focused on identifying energy-dominant spatial structures. In the guide vane region, the leading POD modes highlight significant disturbances on both sides of the blades and the characteristics of the rotating stall. In the runner region, the dominant modes clearly reflect the stall phenomenon induced by dynamic–static interference, effectively capturing the governing flow dynamics in different regions. In contrast, the DMD method excels at extracting frequency-dependent features. In the guide vane area, DMD modes are more localized, with disturbances being concentrated between the fixed and variable guide vanes and near the inlet, resulting in high-frequency vortex structures. In the runner region, the second DMD mode closely matches the first two POD modes and clearly identifies the rotating stall mechanism caused by rotor–stator interference, which is further confirmed through spectral analysis. While some overlap exists between the modal structures of the two methods, the DMD method more effectively captures frequency-driven instabilities, particularly small-scale disturbances and local flow separation, than the POD method. Conversely, the POD method emphasizes energy distribution and global structural patterns. Therefore, the two methods are highly complementary in describing complex flow changes. Specifically, POD aids in identifying dominant energetic structures, whereas DMD reveals their frequency responses and dynamic changes. In combination, these methods provide a comprehensive understanding of the unsteady flow behavior in the hump region from spatial and spectral perspectives.

4. CONCLUSIONS

In this study, the unsteady flow behavior of a pump turbine under hump conditions was investigated through numerical simulation. LES was employed to capture the transient features of turbulence evolution accurately. On the basis of the LES results, POD and DMD were applied to identify and compare key flow structures and instability characteristics. The results demonstrated that both methods effectively extracted energy-dominant modes and clearly revealed the unsteady features associated with the rotating stall mechanism, confirming the reliability and applicability of modal decomposition techniques in analyzing complex flow phenomena. The main conclusions were as follows:

1. Under pump operating conditions, the formation of the hump region is caused primarily by flow instabilities in the guide vane and runner regions. In the guide vane area, instability is attributed mainly to flow separation and vortex formation near the fixed and variable guide vanes. In the runner region, the vortex shedding process between blade passages and the rotating stall process induced by dynamic–static interference in the bladeless zone are the key contributors to unsteady flow behavior.
2. The velocity field of the pump turbine is decomposed via both the POD and DMD methods, yielding modal structures with different flow characteristics. The results reveal the presence of unstable and disordered flow throughout the domain, with alternating velocity disturbance patterns being observed across multiple modes. These interference structures interact to generate vortices that disturb the flow field. A comparative analysis of modal evolution confirms that the rotating stall process in the guide vane region and at the runner outlet is a major factor contributing to hydraulic instability in the hump region.
3. Since the POD method sorts modes on the basis of spatial scales and has spatial orthogonality, its modes may contain multiple frequency components, reflecting the distributions of different flow characteristics. In contrast, the DMD method decomposes flow structures at specific frequencies and exhibits temporal orthogonality, making it suitable for representing the changes in flow behavior. A comparative analysis of modal changes provides guidance for selecting appropriate decomposition methods, enhancing the overall understanding of the flow field decomposition process.

In this study, modal decomposition methods were applied to analyze the unsteady flow structures of a pump turbine operating in the hump region, providing valuable insights into the underlying instability mechanisms. Although high-fidelity LES simulations combined with POD and DMD methods were used to systematically identify dominant modal characteristics, certain limitations remained. These findings included high computational costs and idealized boundary conditions, which could affect the accuracy of capturing details about local flow and nonlinear behaviors. In addition, the current mode ranking was primarily based on energy contributions and would not fully reflect the coupling effects or physical dominance levels among multiple modes. In future research, scholars could incorporate more efficient, multiscale modeling and modal identification techniques, such as spatiotemporal POD (ST–POD), to effectively capture the spatiotemporal changes in the flow field. Integration with experimental validation would further enhance model reliability and support the development of optimized operation and active control strategies for the hump region.

ACKNOWLEDGEMENTS

The authors gratefully acknowledge the financial support from the Open Research Program of the State Key Laboratory of Hydropower Equipment (Grant No. MH20211018).

CONFLICT OF INTEREST

The authors declare that they have no known competing financial interests or personal relationships that could have appeared to influence the work reported in this paper.

AUTHORS CONTRIBUTION

Yuhang Zhang: Conceptualization, Methodology, Formal analysis, Writing original draft, Writing review

and editing; **Junli Wang:** Methodology, Data curation, Conceptualization. **Wentao Su:** Validation, Formal analysis, Data curation. **Yue Zhao:** Methodology, Supervision. **Yuanlin Chen:** Supervision, Project administration, Investigation. **Taiping Chen:** Supervision, Project administration, Methodology. **Jian Wu:** Supervision, Project administration, Methodology, Funding acquisition.

REFERENCES

Arbabi, H., & Mezic, I. (2017). Ergodic theory, dynamic mode decomposition, and computation of spectral properties of the koopman operator. *SIAM Journal on Applied Dynamical Systems*, *16*(4), 2096–2126. https://doi.org/10.1137/17M1125236

Chang, X., & Gao, D. (2023). A comparative study of data-driven modal decomposition analysis of unforced and forced cylinder wakes. *Journal of Visualization*, *26*(4), 755–777. https://doi.org/10.1007/s12650-023-00912-8

Cheng, Y., & Chen, Q. (2021). Large eddy simulation and dynamic mode decomposition of turbulent mixing layers. *Applied Sciences*, *11*(24), 12127. https://doi.org/10.3390/app112412127

Dehghan, A. A., & Shojaeefard, M. H. (2022). Experimental and numerical optimization of a centrifugal pump volute and its effect on head and hydraulic efficiency at the best efficiency point. *Proceedings of the Institution of Mechanical Engineers, Part C: Journal of Mechanical Engineering Science*, *236*(9), 4577–4598. https://doi.org/10.1177/09544062211056019

Dehghan, A. A., Shojaeefard, M. H., & Roshanaei, M. (2024). Exploring a new criterion to determine the onset of cavitation in centrifugal pumps from energy-saving standpoint; experimental and numerical investigation. *Energy*, *293*, 130681. https://doi.org/10.1016/j.energy.2024.130681

François, B., Hingray, B., Raynaud, D., Borga, M., & Creutin, J. D. (2016). Increasing climate-related-energy penetration by integrating run-of-the river hydropower to wind/solar mix. *Renewable Energy*, *87*, 686–696. https://doi.org/10.1016/j.renene.2015.10.064

Han, Y., & Tan, L. (2020). Dynamic mode decomposition and reconstruction of tip leakage vortex in a mixed flow pump as turbine at pump mode. *Renewable Energy*, *155*, 725–734. https://doi.org/10.1016/j.renene.2020.03.142

Hao, Z., Shi, G., Peng, X., Chai, H., Lv, W., & Huang, Z. (2024). Study on the influence of vortex spatial-temporal evolution on the causes of hump region of Pump-Turbine and the characteristics of vortex dynamics. *Journal of Energy Storage*, *92*, 112297. https://doi.org/10.1016/j.est.2024.112297

Heng, Y., Yuan, S., Hong, F., Yuan, J., Si, Q., & Hu, B. (2014). *A hybrid method for flow-induced noise in centrifugal pumps based on LES and FEM.* Proceedings of the ASME Fluids Engineering Division Summer Meeting, 2013, 1b: Symposia, V01BT10A034.

Jin, F., Luo, Y., Bi, H., Wang, H., Wang, Z., Lin, K., Lei, X., & Yang, X. (2023). Transient simulation of reversible pump turbine during pump mode's starting up. *Journal of Energy Storage*, *68*, 107678. https://doi.org/10.1016/j.est.2023.107678

Karapici, V., Trojer, A., Lazarevikj, M., Pluskal, T., Chernobrova, A., Neziric, E., Zuecco, G., Alerci, A. L., Seydoux, M., Doujak, E., & Rudolf, P. (2024). Opportunities of hidden hydropower technologies towards the energy transition. *Energy Reports*, *12*, 5633–5647. https://doi.org/10.1016/j.egyr.2024.11.039

Lai, X., Chen, X., Liang, Q., Ye, D., Gou, Q., Wang, R., & Yan, Y. (2023). Experimental and numerical investigation of vortex flows and pressure fluctuations in a high-head pump-turbine. *Renewable Energy*, *211*, 236–247. https://doi.org/10.1016/j.renene.2023.04.092

Li, D., Wang, H., Qin, Y., Wei, X., & Qin, D. (2018). Numerical simulation of hysteresis characteristic in the hump region of a pump-turbine model. *Renewable Energy*, *115*, 433–447. https://doi.org/10.1016/j.renene.2017.08.081

Liang, A., Li, H., Zhang, W., Yao, Z., Zhu, B., & Wang, F. (2024). Study on pressure fluctuation and rotating stall characteristics in the vaneless space of a pump-turbine in pump mode. *Journal of Energy Storage*, *94*, 112385. https://doi.org/10.1016/j.est.2024.112385

Liang, W., Chen, T., Wang, G., & Huang, B. (2020). Investigation of unsteady liquid nitrogen cavitating flows with special emphasis on the vortex structures using mode decomposition methods. *International Journal of Heat and Mass Transfer*, *157*, 119880. https://doi.org/10.1016/j.ijheatmasstransfer.2020.119880

Liao, Z. Y., Yang, J., Liu, X. H., Hu, W. L., & Deng, X. R. (2020). Analysis of unsteady flow structures in a centrifugal impeller using proper orthogonal decomposition. *Journal of Applied Fluid Mechanics*, *14*(1), 89–101. https://doi.org/10.47176/jafm.14.01.31299

Liu, D., Xun, H., Wang, Z., Li, G., Zheng, J., Liu, X., & Hao, Z. (2024). Analysis of vortex characteristics in hump region of reversible pump-turbine based on omega vortex identification method. *AIP Advances*, *14*(3), 035130. https://doi.org/10.1063/5.0199021

Liu, M., Tan, L., & Cao, S. (2019a). Dynamic mode decomposition of cavitating flow around ALE 15 hydrofoil. *Renewable Energy*, *139*, 214–227. https://doi.org/10.1016/j.renene.2019.02.055

Liu, M., Tan, L., & Cao, S. (2019b). Dynamic mode decomposition of gas-liquid flow in a rotodynamic multiphase pump. *Renewable Energy*, *139*, 1159–1175. https://doi.org/10.1016/j.renene.2019.03.015

Long, Y., Guo, X., & Xiao, T. (2024). Research, application and future prospect of mode decomposition in fluid mechanics. *Symmetry*, *16*(2), 155. https://doi.org/10.3390/sym16020155

Lu, J., Qian, Z., & Lee, Y. H. (2021). Numerical investigation of unsteady characteristics of a pump turbine under runaway condition. *Renewable Energy*, *169*, 905–924. https://doi.org/10.1016/j.renene.2021.01.063

Lumley, J. L. (1967). The structure of inhomogeneous turbulent flows. *Atmospheric turbulence and radio wave propagation, Journal of Computational Chemistry*, *23* (13), 1236–1243. http://citeseer.uark.edu:8080/citeseerx/showciting;jsessionid=D3D18DF04BF1E9304E98A88B3DFDD699?cid=3063452

Magionesi, F., Dubbioso, G., Muscari, R., & Mascio, A. D. (2018). Modal analysis of the wake past a marine propeller. *Journal of Fluid Mechanics*, *855*, 469–502. https://doi.org/10.1017/jfm.2018.631

Mahfoud, R. J., Alkayem, N. F., Zhang, Y., Zheng, Y., Sun, Y., & Alhelou, H. H. (2023). Optimal operation of pumped hydro storage-based energy systems: A compendium of current challenges and future perspectives. *Renewable and Sustainable Energy Reviews*, *178*, 113267. https://doi.org/10.1016/j.rser.2023.113267

Mariappan, S., Gardner, A. D., Richter, K., & Raffel, M. (2014). Analysis of dynamic stall using dynamic mode decomposition technique. *AIAA Journal*, *52*(11), 2427–2439. https://doi.org/10.2514/1.J052858

Mohsin, M., Orynbassarov, D., Anser, M. K., & Oskenbayev, Y. (2023). Does hydropower energy help to reduce CO2 emissions in European Union countries? Evidence from quantile estimation. *Environmental Development*, *45*, 100794. https://doi.org/10.1016/j.envdev.2022.100794

Muld, T. W., Efraimsson, G., & Henningson, D. S. (2012). Flow structures around a high-speed train extracted using proper orthogonal decomposition and dynamic mode decomposition. *Computers & Fluids*, *57*, 87–97. https://doi.org/10.1016/j.compfluid.2011.12.012

Nasir, J., Javed, A., Ali, M., Ullah, K., & Kazmi, S. A. A. (2022). Capacity optimization of pumped storage hydropower and its impact on an integrated conventional hydropower plant operation. *Applied Energy*, *323*, 119561. https://doi.org/10.1016/j.apenergy.2022.119561

Proctor, J. L., Brunton, S. L., & Kutz, J. N. (2016). Dynamic mode decomposition with control. *SIAM Journal on Applied Dynamical Systems*, *15*(1), 142–161. https://doi.org/10.1137/15M1013857

Qin, Y., Li, D., Wang, H., Liu, Z., Wei, X., & Wang, X. (2023). Mechanism of runner high-pressure side on stall characteristics at typical unsteady operating points in both modes of a pump turbine. *Physics of Fluids*, *35*(7), 074102. https://doi.org/10.1063/5.0155655

Renhui, Z., Chen, X., & Luo, J. (2020). Knowledge mining of low specific speed centrifugal pump impeller based on proper orthogonal decomposition method. *Journal of Thermal Science*, *30*. https://doi.org/10.1007/s11630-020-1356-5

Rowley, C. W., & Dawson, S. T. M. (2017). Model reduction for flow analysis and control. *Annual Review of Fluid Mechanics, 49*, 387-417. https://doi.org/10.1146/annurev-fluid-010816-060042

Schmid, P. J. (2010). Dynamic mode decomposition of numerical and experimental data. *Journal of Fluid Mechanics*, *656*, 5–28. https://doi.org/10.1017/S0022112010001217

Schmid, P. J. (2022). Dynamic mode decomposition and its variants. *Annual Review of Fluid Mechanics*, *54*, 225–254. https://doi.org/10.1146/annurev-fluid-030121-015835

Sieber, M., Paschereit, C. O., & Oberleithner, K. (2016). Spectral proper orthogonal decomposition. *Journal of Fluid Mechanics*, *792*, 798–828. https://doi.org/10.1017/jfm.2016.103

Sirovich, L. (1987). Turbulence and the dynamics of coherent structures. I. Coherent structures. *Quarterly of Applied Mathematics*, *45*, 561–571. https://doi.org/10.1090/qam/910462

Subramanya, K., & Chelliah, T. R. (2023). Capability of synchronous and asynchronous hydropower generating systems: A comprehensive study. *Renewable and Sustainable Energy Reviews*, *188*, 113863. https://doi.org/10.1016/j.rser.2023.113863

Taira, K., Brunton, S. L., Dawson, S. T. M., Rowley, C. W., Colonius, T., McKeon, B. J., Schmidt, O. T., Gordeyev, S., Theofilis, V., & Ukeiley, L. S. (2017). Modal analysis of fluid flows: An overview. *AIAA Journal*, *55*(12), 4013–4041. https://doi.org/10.2514/1.J056060

Taira, K., Hemati, M. S., Brunton, S. L., Sun, Y., Duraisamy, K., Bagheri, S., Dawson, S. T. M., & Yeh, C.-A. (2020). Modal analysis of fluid flows: applications and outlook. *AIAA Journal*, *58*(3), 998–1022. https://doi.org/10.2514/1.J058462

Towne, A., Schmidt, O. T., & Colonius, T. (2018). Spectral proper orthogonal decomposition and its relationship to dynamic mode decomposition and resolvent analysis. *Journal of Fluid Mechanics, 847*, 821–867. https://doi.org/10.1017/jfm.2018.283

Wang, Z., Fang, G., Wen, X., Tan, Q., Zhang, P., & Liu, Z. (2023a). Coordinated operation of conventional hydropower plants as hybrid pumped storage hydropower with wind and photovoltaic plants. *Energy Conversion and Management*, *277*, 116654. https://doi.org/10.1016/j.enconman.2022.116654

Wang, J., Wang, C., Liu, C., & Wu, J. (2023b). *Numerical study on stall characteristics of a triangular airfoil in* *low Reynolds number compressible flow.* 17th Asian Congress of Fluid Mechanics (ACFM 2023), 2023, 182–189. https://doi.org/10.1049/icp.2023.1947

Williams, M. O., Kevrekidis, I. G., & Rowley, C. W. (2015). A data-driven approximation of the koopman operator: extending dynamic mode decomposition. *Journal of Nonlinear Science*, *25*(6), 1307–1346. https://doi.org/10.1007/s00332-015-9258-5

Wu, H. (2023). Evaluating the role of renewable energy investment resources and green finance on the economic performance: Evidence from OECD economies. *Resources Policy*, *80*, 103149. https://doi.org/10.1016/j.resourpol.2022.103149

Xu, L., Kan, K., Zheng, Y., Liu, D., Binama, M., Xu, Z., Yan, X., Guo, M., & Chen, H. (2024a). Rotating stall mechanism of pump-turbine in hump region: An insight into vortex evolution. *Energy*, *292*, 130579. https://doi.org/10.1016/j.energy.2024.130579

Yang, J., Feng, X., Liao, Z., Pan, K., & Liu, X. (2023). Analysis on the mechanism of rotating stall inner a pump turbine in pump mode based on the proper orthogonal decomposition. *Journal of Fluids Engineering*, *145* (9), 091202. https://doi.org/10.1115/1.4062345

Yang, Z., Wang, F., & Zhou, P. (2012). Evaluation of subgrid-scale models in large-eddy simulations of turbulent flow in a centrifugal pump impeller. *Chinese Journal of Mechanical Engineering*, *25*(5), 911–918. https://doi.org/10.3901/CJME.2012.05.911

Ye, W., Qian, Z., Zeng, Y., Ma, W., Geng, X., Luo, X., & Wang, H. (2024). Numerical investigation on the unstable flow and its interaction with the hump characteristic in a pump turbine at pump mode. *Journal of Energy Storage*, *101*, 113853. https://doi.org/10.1016/j.est.2024.113853

Yin, X., Huang, X., Zhang, S., Bi, H., & Wang, Z. (2023). Numerical investigation of flow and structural characteristics of a large high-head prototype pump-turbine during turbine start-up. *Energies*, *16*(9), 3743. https://doi.org/10.3390/en16093743

Zhang, F., Chen, Z., Han, S., & Zhu, B. (2024). Study on the unsteady flow characteristics of a pump turbine in pump mode. *Processes*, *12*(1), 41. https://doi.org/10.3390/pr12010041

Zheng, Y., Tang, K., Xu, L., Ren, S., Xu, J., Wang, Y., An, D., & Ye, C. (2024). Stability analysis of pump-turbine in hump zone based on omega vortex identification method. *Water*, *16*(23), 3443. https://doi.org/10.3390/w16233443